

## Corrosion and passive film characteristics of 3D-printed NiTi shape memory alloys in artificial saliva

Liu, Ming; Zhu, Jia Ning; Popovich, V. A.; Borisov, E.; Mol, J. M.C.; Gonzalez-Garcia, Y.

**DOI**

[10.1007/s12598-023-02329-6](https://doi.org/10.1007/s12598-023-02329-6)

**Publication date**

2023

**Document Version**

Final published version

**Published in**

Rare Metals

**Citation (APA)**

Liu, M., Zhu, J. N., Popovich, V. A., Borisov, E., Mol, J. M. C., & Gonzalez-Garcia, Y. (2023). Corrosion and passive film characteristics of 3D-printed NiTi shape memory alloys in artificial saliva. *Rare Metals*, 42(9), 3114-3129. <https://doi.org/10.1007/s12598-023-02329-6>

**Important note**

To cite this publication, please use the final published version (if applicable).  
Please check the document version above.

**Copyright**

Other than for strictly personal use, it is not permitted to download, forward or distribute the text or part of it, without the consent of the author(s) and/or copyright holder(s), unless the work is under an open content license such as Creative Commons.

**Takedown policy**

Please contact us and provide details if you believe this document breaches copyrights.  
We will remove access to the work immediately and investigate your claim.



# Corrosion and passive film characteristics of 3D-printed NiTi shape memory alloys in artificial saliva

Ming Liu\*, Jia-Ning Zhu, V. A. Popovich, E. Borisov, J. M. C. Mol, Y. Gonzalez-Garcia

Received: 28 October 2022 / Revised: 18 November 2022 / Accepted: 10 December 2022 / Published online: 27 June 2023  
© The Author(s) 2023

**Abstract** Electrochemical tests and surface analysis were applied to study the corrosion behavior and passive film characteristics of three-dimensional-printed NiTi shape memory alloys fabricated by laser-powder bed fusion (L-PBF) in artificial saliva at 37 °C. The passivity of L-PBF NiTi shows to be influenced by the process parameters and resulting morphological and physicochemical surface properties. The results show that the defects at the surface of L-PBF NiTi can promote the passivation rate in the early stages of exposure but a slowly formed passive film shows the best corrosion protection. The thickness of the passive film is positively correlated with its corrosion protective performance. The L-PBF NiTi alloy prepared at a linear energy density of  $0.2 \text{ J}\cdot\text{m}^{-1}$  and volumetric energy density of  $56 \text{ J}\cdot\text{mm}^{-3}$  shows the least defects and best corrosion protection. An outer Ti-rich and inner Ni-rich dense passive film could be also obtained showing higher corrosion resistance.

**Keywords** NiTi; Laser-powder bed fusion (L-PBF); Passive film; Corrosion resistance; Artificial saliva

## 1 Introduction

NiTi shape memory alloys (SMA) have been widely used in the field of clinical stomatology, such as arch wire [1, 2], bracket in orthodontic treatments [3] and root canal files [4]. Human saliva is a variable solution containing a variety of electrolyte constituents. This and many other factors such as (local) pH, microbial activity and mechanical loads in saliva could all affect the corrosion process of NiTi-SMA [1–5]. Hence, depending on the electrolyte conditions, NiTi-SMA may be subjected to corrosion through electrochemical activity in human salivary and human body fluid environment. Also, the release of Ni ions may cause allergic reactions and other adverse effects in human body [6–8].

The corrosion resistance of NiTi-SMA in saliva is mainly related to its passive film, which can be spontaneously formed in air and electrolytes with a thickness of 2–10 nm mainly containing  $\text{TiO}_2$  protecting the underlying substrate from corrosion [9, 10]. However, microorganisms, food composition, pH and stress may reduce the stability of the passive film, resulting in increased Ni ion release rate and clinical symptoms [11]. Through electrochemical testing, Mirjalili et al. [12] found that no obvious pitting corrosion could be observed on NiTi-SMA in artificial saliva, in contrast with obvious corrosion pit formation in SS304 stainless steel. A pre-passivation treatment could improve the corrosion resistance of NiTi-SMA in fluoride-containing artificial saliva. Mocnik et al. [13] also showed that the decrease in pH and the increase in fluoride concentration in artificial saliva could both reduce the corrosion resistance of NiTi-SMA. Masjedi et al. [14] analyzed the corrosion data of NiTi-SMA arch wire used by persons of different gender and age for various times through double-blind parallel randomized clinical trial. The

M. Liu\*  
State Key Laboratory for Mechanical Behavior of Materials,  
Center for Advancing Materials Performance from the  
Nanoscale (CAMP-Nano), Xi'an Jiaotong University, Xi'an  
710049, China  
e-mail: liuming0313@xjtu.edu.cn

M. Liu, J.-N. Zhu, V. A. Popovich, J. M. C. Mol,  
Y. Gonzalez-Garcia  
Department of Materials Science and Engineering, Delft  
University of Technology, AA Delft 2600, The Netherlands

E. Borisov  
Peter the Great Saint-Petersburg Polytechnic University, Saint  
Petersburg 195251, Russia



results showed that the Ni ions content of NiTi-SMA in saliva increased from  $(10.46 \pm 0.77)$  to  $(11.078 \pm 0.81) \mu\text{g}\cdot\text{L}^{-1}$  after 2 months of immersion, showing a significant statistical difference. Age and gender had no significant correlation with the Ni ion release rate. The statistical differences of NiTi-SMA, Cu-NiTi-SMA and epoxy-NiTi-SMA were  $(0.83 \pm 0.14)$ ,  $(0.65 \pm 0.10)$  and  $(0.39 \pm 0.11) \mu\text{g}\cdot\text{L}^{-1}$ , showing that using epoxy-NiTi-SMA could reduce the Ni ion release rate.

Currently, the applicability of intricately shaped NiTi-SMA is severely limited due to its poor manufacturability [5]. In recent years, with the development of three-dimensional (3D)-printing (also known as additive manufacturing) technology, the challenges and drawbacks of traditional subtractive manufacturing can be effectively avoided [15–17]. Khoo et al. [18] reviewed the recent progress of NiTi-SMA manufactured by selective laser melting and found that the preparation of NiTi-SMA by 3D printing was more challenging than that of the traditional process. Marattukalam et al. [19] studied the influence of laser power on the corrosion rate of NiTi-SMA in Ring's solution and found that the corrosion rate decreased with the increase in laser power. Grain boundaries of 3D-printed NiTi-SMA showed the weakest corrosion resistance [15, 19], the corrosion resistance of the alloy could be greatly improved by the reduction of the number of grain boundaries per unit of volume.

In this work, corrosion properties and passive film characteristics of the three NiTi-SMA prepared by laser-powder bed fusion (L-PBF NiTi) with various processing parameters (laser power, scanning velocity, hatch distance and layer thickness) were studied. The corrosion properties and passivity of three L-PBF NiTi in artificial saliva were systematically studied by means of electrochemical techniques to identify the passive film properties for different L-PBF manufacturing process conditions and combined with surface analysis to further determine the passive film characteristics.

## 2 Experimental

### 2.1 Material

NiTi-SMA specimens with same Ni:Ti atomic number ratio were produced by laser-powder bed fusion using the process parameters shown in Table 1. In our previous study, L-PBF NiTi-SMA with various types of defects (cracks, keyhole induced porosities and free defect) were fabricated by applying different sets of processing parameters (laser power, scanning velocity, hatch distance and layer thickness) [20]. To estimate co-effects of different processing parameter combinations on single laser bead

**Table 1** L-PBF manufacturing parameters of NiTi

Sample	A2	A4	A6
Laser power / W	250	250	250
Scanning velocity / ( $\text{mm}\cdot\text{s}^{-1}$ )	1250	800	500
Hatch distance / m	120	120	140
Layer thickness / m	30	30	60
Laser beam size / m	80	80	80
Linear energy density / ( $\text{J}\cdot\text{mm}^{-1}$ )	0.2	0.3	0.5
Volumetric energy density / ( $\text{J}\cdot\text{mm}^{-3}$ )	56	87	60

and component, two metrics of linear energy density ( $E_l$ ,  $\text{J}\cdot\text{mm}^{-1}$ ) and volumetric energy density ( $E_v$ ,  $\text{J}\cdot\text{mm}^{-3}$ ) were used. The definition of  $E_l$  is expressed in Eq. (1):

$$E_l = \frac{P}{v} \quad (1)$$

and the  $E_v$  is defined by Eq. (2):

$$E_v = \frac{P}{v \times h \times t} \quad (2)$$

where  $P$  is the laser power (W),  $v$  is the scanning velocity ( $\text{mm}\cdot\text{s}^{-1}$ ),  $h$  is hatch distance ( $\mu\text{m}$ ) and  $t$  is layer thickness ( $\mu\text{m}$ ). To maintain consistency with our previous work, the same sample groups were used in this work, i.e., A2 ( $56 \text{ J}\cdot\text{mm}^{-3}$ ), A4 ( $87 \text{ J}\cdot\text{mm}^{-3}$ ) and A6 ( $60 \text{ J}\cdot\text{mm}^{-3}$ ) [20]. The printed samples have a cylindrical shape with a dimension of  $\Phi 6 \text{ mm} \times 10 \text{ mm}$ . For the electrochemical experiments, the samples were cut in sheets of  $\Phi 6 \text{ mm} \times 3 \text{ mm}$ , and for the surface analysis, the dimension was  $\Phi 6 \text{ mm} \times 2 \text{ mm}$ . Before the experiments, all samples were polished from grit #200 to #2000 step by step with SiC sandpaper, cleaned and dried with alcohol and deionized water.

### 2.2 Electrochemical characterization

The one circular side of the electrochemical sample was connected with a conductor and conductive adhesive, and the rest was sealed with epoxy resin to retain a working area of  $0.28 \text{ cm}^2$ . The standard three-electrode cell was used for the electrochemical tests. The cell consisted of a platinum plate ( $10 \text{ cm}^2$ ) as the counter electrode, a saturated calomel electrode (SCE) as the reference and the samples as the working electrode. Experiments were performed on a Biologic VMP3 multi-channel electrochemical workstation.

The electrolyte used for the electrochemical experiments was the modified Fusayama artificial saliva with the pH of approximately 7 [6, 7, 13]. This solution consisted of a mix of KCl ( $400 \text{ mg}\cdot\text{L}^{-1}$ ), NaCl ( $400 \text{ mg}\cdot\text{L}^{-1}$ ),  $\text{CaCl}_2\cdot 2\text{H}_2\text{O}$  ( $795 \text{ mg}\cdot\text{L}^{-1}$ ), KSCN ( $300 \text{ mg}\cdot\text{L}^{-1}$ ),

$\text{Na}_2\text{S}\cdot 9\text{H}_2\text{O}$  ( $5\text{ mg}\cdot\text{L}^{-1}$ ),  $\text{NaH}_2\text{PO}_4\cdot\text{H}_2\text{O}$  ( $690\text{ mg}\cdot\text{L}^{-1}$ ) and urea ( $1000\text{ mg}\cdot\text{L}^{-1}$ ). The solution was prepared using analytical pure chemical reagent and deionized water. The volume of the artificial saliva for electrochemical test was 500 ml, and the pH was monitored every day, if the pH value changed beyond the range, a fresh solution would be replaced.

The open circuit potential (OCP) was continuously monitored for 168 h. The scanning range of potentiodynamic polarization curve was from the cathodic ( $-250\text{ mV}$  vs. OCP) to the anodic range at a scan rate of  $1\text{ mV}\cdot\text{s}^{-1}$ ; the scanning stopped when the anode current density exceeded  $1\text{ mA}\cdot\text{cm}^{-2}$ . The cyclic voltammetry (CV) test was carried out in three potential ranges:  $-2.0$ – $2.0$ ,  $-1.5$ – $1.5$  and  $-1.0$ – $1.0\text{ V}$  (vs. SCE), the initial positive scanning was from the negative potential and then back to the initial potential, a total of 5 cycles were carried out with a scanning rate of  $100\text{ mV}\cdot\text{s}^{-1}$ . Electrochemical impedance spectroscopy (EIS) was carried out at OCP conditions. The frequency range was  $100\text{ kHz}$ – $10\text{ mHz}$ , the sine wave signal amplitude was  $10\text{ mV}$ . The data were analyzed and fitted by using the ZsimpWin 3.5 software. The test frequency in the Mott–Schottky analysis was fixed at  $1\text{ kHz}$ , the scan rate was  $50\text{ mV}\cdot\text{s}^{-1}$  and the scanning potential range was  $-1.0$  to  $+1.5\text{ V}$  (vs. SCE). All the electrochemical measurements were performed at least three times, and the representative results were given in this work. The electrolyte temperature for all electrochemical measurements was controlled at  $(37 \pm 0.5)^\circ\text{C}$  by a thermostatic electric water bath.

### 2.3 Auger electron spectroscopy measurements

The through-thickness passive film composition of three L-PBF NiTi alloys after immersion in artificial saliva for 168 h was analyzed by Auger electron spectroscopy (AES). The nano scanning Auger system model PHI-700 (Ulvac-PHI, Japan) was used. The detection was based on general principles of AES analysis methods (GB/T 26,533—2011). A coaxial electron gun and cylindrical mirror analyzer (CMA) were used. The beam voltage was  $5\text{ kV}$ , and the energy resolution was  $1\%$ . The incident angle was  $30^\circ$ , and the vacuum degree of the analysis chamber was better than  $5.1 \times 10^{-12}\text{ MPa}$ . The passive films were etched by  $\text{Ar}^+$  ions with a  $\Phi 100\text{ nm}$  spot to obtain the depth profiles, the sputtering rate was  $1\text{ nm}\cdot\text{min}^{-1}$ , determined by the thermal oxidation of a  $\text{SiO}_2/\text{Si}$  standard.

### 2.4 X-ray photoelectron spectroscopy measurements

The passive film compositions of three L-PBF NiTi alloys after immersion in artificial saliva for 168 h were analyzed by X-ray photoelectron spectroscopy (XPS). In the test, the

monochromator was  $\text{Al K}\alpha$ , the sensitivity was 100 kilocycles per second (Kcps), the energy spectrum scanning range was  $0$ – $1350\text{ eV}$ , the wide and narrow scanning intervals were  $1$  and  $0.1\text{ eV}$ , respectively. The energy spectrum was calibrated by  $\text{C 1s}$  ( $285.0\text{ eV}$ ). Element type and content were analyzed by comparison with standard element spectra (Perkin-Elmer's XPS Data Sheet and XPS International Inc. website). Through analysis of the outer and inner passive film composition of L-PBF NiTi, the differences in composition and structure of their respective passive film were further studied. XPSPeak 4.1 software was used to analyze data by Gauss–Newton fitting.

### 2.5 Ni ion release test

The Ni ion release rate of three L-PBF NiTi alloys after immersion in artificial saliva for 168 h was determined by an inductively coupled plasma mass spectrometer (ICP-MS). During the immersion, all samples were sealed to an exposed area of  $0.28\text{ cm}^2$  and immersed in 100-ml artificial saliva. The Ni ion concentration was measured by an ICP-MS (NexION 350D, USA) system, the corresponding wavelength of Ni was  $233.7\text{ nm}$ .

## 3 Results and discussion

### 3.1 Microstructure and surface morphology

Microstructures of L-PBF NiTi fabricated with various energy densities and defects are shown in Fig. 1. The defect-free A2 sample shows densely packed laser beads and a conduction mode melt pool shape from the cross-sectional view along the building direction (Fig. 1a). As shown in the enlarged zone of A2 (Fig. 1d), columnar grains grow along the building direction and can extend beyond melt pool boundaries, indicating a directional thermal gradient and epitaxial grain growth. With increasing linear energy density ( $E_l$ ) from  $0.2$  to  $0.3\text{ J}\cdot\text{mm}^{-1}$  (Table 1), deeper melt pools and cracks formed in the A4 sample are observed (Fig. 1b and e). It is noted that cracks propagate along the building direction. Considering the columnar grain growth along building direction in L-PBF NiTi, the crack formation should be attributed to intergranular cracking induced by thermal shrinkage. Further increase in  $E_l$  to  $0.5\text{ J}\cdot\text{mm}^{-1}$  for the A6 sample results in even deeper melt pools with keyhole mode. Due to the large depth-to-width ratio of the melt pool in A6 sample, melt pool fluid is unstable and can easily collapse to induce gas pores or porosities in the bottom of the melt pool (Fig. 1c and f) [21]. More details about melt pool shape evolution and defect formation mechanism can be found in our previous work [20].



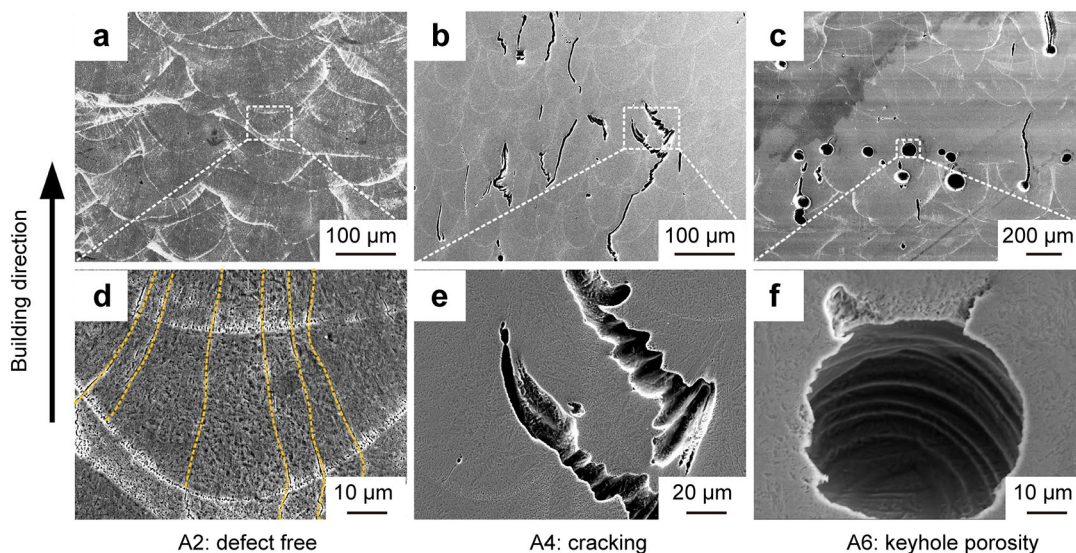


**Fig. 1** Optical microscope (OM) images of L-PBF NiTi fabricated with different structural defects: **a, d** A2 ( $56 \text{ J}\cdot\text{mm}^{-3}$ ), **b, e** A4 ( $87 \text{ J}\cdot\text{mm}^{-3}$ ) and **c, f** A6 ( $60 \text{ J}\cdot\text{mm}^{-3}$ )

However, its effects on electrochemical behavior remain to be investigated in this study.

## 3.2 Electrochemical analysis

### 3.2.1 Open circuit potential

The formation rate of a passive film in the early stages of exposure can be characterized by the OCP variation [22, 23]. Figure 2a shows the OCPs of three L-PBF NiTi after immersion in artificial saliva for 30 min. It can be seen that the OCPs of the L-PBF NiTi increase rapidly for all the samples, but the rate of increase is rather different for different samples. The formation rate of the L-PBF NiTi passive films can be determined [23]:

$$E = \text{const.} + 2.303\delta^- / A \lg t \quad (3)$$

where  $\delta^-$  is the passive film growth rate at  $\lg t$ , and  $A$  is a constant which can be calculated by the following equation [23]:

$$A = \frac{nF}{RT} \alpha \delta' \quad (4)$$

where  $\alpha$  is the charge transfer coefficient ( $\alpha = 0.5$ ) [23],  $n$  is the valence state ( $n = 2$ ),  $F$  is Faraday's constant ( $9.65 \times 10^4 \text{ C}\cdot\text{mol}^{-1}$ ),  $R$  is the gas constant ( $8.314 \text{ J}\cdot\text{mol}^{-1}\cdot\text{K}^{-1}$ ),  $T$  is the thermodynamic temperature and  $\delta'$  represents the energy accumulation width during charge transfer ( $\delta' = 1$ ). Earlier studies reported that the passive film of NiTi was mainly  $\text{TiO}_2$  [8, 9], which was in line with our own AES and XPS results reported later in this study. Thus, we may assume that the thickness of L-PBF NiTi passive film in artificial saliva increases mainly

through  $\text{Ti}^{4+}$  diffusion to the interface between Ti and oxygen. The value of  $n$  in Eq. (2) is 4, and the calculated  $A$  is  $78 \text{ nm}\cdot\text{V}^{-1}$ . Then, the OCP vs.  $t$  could be transformed into  $V$  vs.  $1/\lg t$  (see Fig. 2b); hence, the early stage passive film growth rate  $\delta^-$  of three L-PBF NiTi can be calculated by Eq. (1). Figure 2c shows that the early stage passive film formation rate from high to low is:  $A6 > A4 > A2$ ; the rate for A6 is about 4 times higher than that of A2 and two times of that of A4.

In order to study the long-term passive film formation process of L-PBF NiTi in artificial saliva, the OCPs of three L-PBF NiTi were continuously tested in artificial saliva for 168 h, as shown in Fig. 2d. It can be seen that the OCPs of the three alloys increase rapidly at the initial stage of immersion and then rather stabilize. The OCP values for A2 increase from  $-288$  (30 min) to  $-175 \text{ mV}$  (vs. SCE) (6 h) and then slowly stabilize to approx.  $-156 \text{ mV}$  (vs. SCE) after immersion for 12 h. The OCP of A4 increases from  $-323$  (30 min) to  $-172 \text{ mV}$  (vs. SCE) for 6 h immersion and then stabilizes to about  $-125 \text{ mV}$  (vs. SCE) after immersion for 12 h. The OCP of A6 increases from about  $-277$  (30 min) to  $-96 \text{ mV}$  (vs. SCE) after immersion for 6 h and then stabilizes at about  $-35 \text{ mV}$  (vs. SCE) (24 h). After immersion for 168 h, the stable OCP values of the three L-PBF NiTi from the positive to negative are according to the order  $A6 > A4 > A2$ .

### 3.2.2 Potentiodynamic polarization

The potentiodynamic polarization characteristics of the L-PBF NiTi alloys were analyzed at two different time of immersion, (i) soon after the rapid OCP value increase in the early stages of immersion (0.5 h) and (ii) after

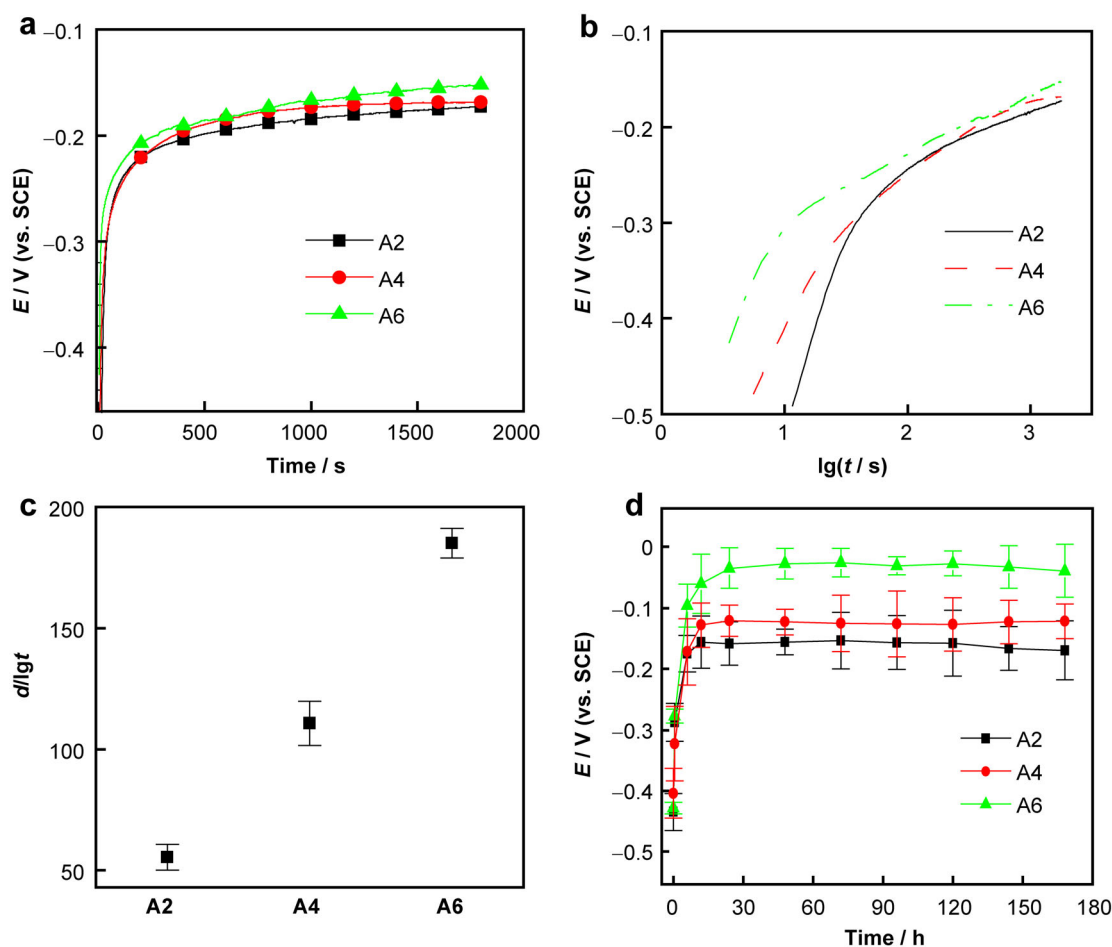


**Fig. 2** **a** OCPs of L-PBF NiTi after immersion in artificial saliva for 1800 s, **b**  $E$  vs.  $\lg t$  and **c** passive film thickness  $d$  (nm) vs.  $\lg t$  (s); **d** OCPs of L-PBF NiTi after immersion in artificial saliva for 168 h

immersion for 48 h. Figure 3a–c shows the potentiodynamic polarization curves of L-PBF NiTi immersed in artificial saliva for 0.5 and 48 h. The polarization curves of all three L-PBF NiTi samples immersed for 0.5 and 48 h all show the characteristics of typical passivation with a wide passive region [22]. The anodic polarization curves of L-PBF NiTi enter the passivation region without obvious activation–passivation transition characteristics.

Indicative potential and current density values and slopes deduced from the potentiodynamic polarization curves are listed in Table 2. It can be seen that A2 has a relatively negative corrosion potential ( $E_{\text{corr}}$ ), which is consistent with the OCP test results. In order to compare the maintaining passivity ( $i_{\text{pass}}$ ), the current density when the anode potential equals 0.60 V (vs. SCE) was used for comparison. The order of the corrosion current density ( $i_{\text{corr}}$ ) from low to high is:  $A6 < A4 < A2$  for the 0.5 h-immersed and  $A2 < A4 < A6$  for the 48 h-immersed samples (see Table 2 and Fig. 3d). The corrosion current density values for all samples decrease significantly as a function of immersion time from 0.5 to 48 h. The limited

corrosion resistance of L-PBF NiTi in the early stages of immersion may be related to the relatively limited extent and integrity of the passive film formation at that stage, which is consistent with the test result of OCPs in Fig. 2d. However, the sequence of the corrosion resistance reverses ( $A2 > A4 > A6$ ) after 48 h of immersion, which is positively correlated with the initial surface quality (Fig. 1), and A2 shows the lowest and A6 shows the highest corrosion current density. In addition, after 48 h of immersion, A2 shows the lowest passive current density as compared to A4 and A6, indicating higher protectiveness of the passive film formed on A2 as compared to that on A4 and A6 at prolonged immersion time.

### 3.2.3 Cyclic voltammetry curve

Figure 4 shows the cyclic voltammetry curves of the three L-PBF NiTi alloys immersed in artificial saliva for 30 min. In order to distinguish the possible redox reactions, three scanning potential ranges were selected:  $-2.0$ – $2.0$ ,  $-1.5$ – $1.5$  and  $-1.0$ – $1.0$  V (vs. SCE). From the wide range

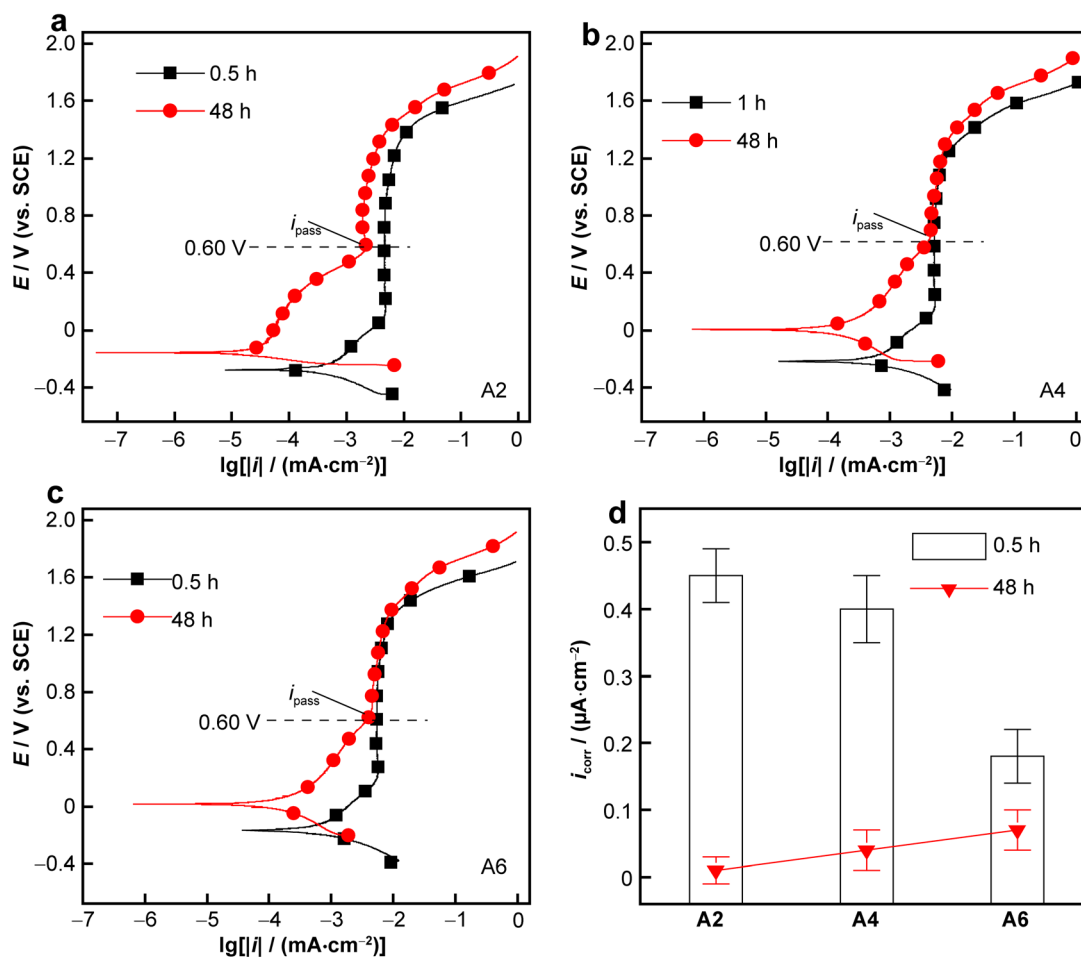
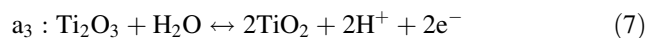
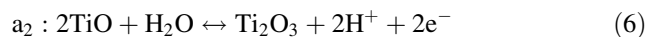
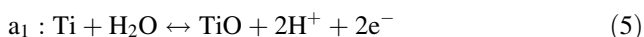


**Fig. 3** Potentiodynamic polarization curves of L-PBF NiTi after immersion in artificial saliva for 0.5 and 48 h: **a** A2 ( $56 \text{ J}\cdot\text{mm}^{-3}$ ), **b** A4 ( $87 \text{ J}\cdot\text{mm}^{-3}$ ), **c** A6 ( $60 \text{ J}\cdot\text{mm}^{-3}$ ) and **d**  $i_{\text{corr}}$

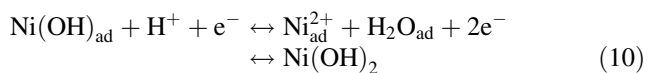
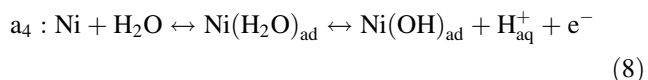
**Table 2** Polarization curve parameter values of L-PBF NiTi after immersion in artificial saliva for 0.5 and 48 h

Sample	$E_{\text{corr}} / \text{mV (vs. SCE)}$	$i_{\text{corr}} / (\mu\text{A}\cdot\text{cm}^{-2})$	$b_a / (\text{mV}\cdot\text{dec}^{-1})$	$b_c / (\text{mV}\cdot\text{dec}^{-1})$	$i_{\text{pass}} / (\mu\text{A}\cdot\text{cm}^{-2})$
A2 (0.5 h)	$-276 \pm 12$	$0.45 \pm 0.04$	$275 \pm 12$	$-153 \pm 8$	$5.7 \pm 0.5$
A2 (48 h)	$-154 \pm 8$	$0.01 \pm 0.02$	$315 \pm 14$	$-136 \pm 6$	$2.0 \pm 0.3$
A4 (0.5 h)	$-219 \pm 13$	$0.40 \pm 0.05$	$274 \pm 11$	$-145 \pm 7$	$5.5 \pm 0.7$
A4 (48 h)	$1 \pm 7$	$0.04 \pm 0.03$	$283 \pm 13$	$-149 \pm 4$	$4.7 \pm 0.4$
A6 (0.5 h)	$-175 \pm 14$	$0.18 \pm 0.04$	$272 \pm 10$	$-142 \pm 7$	$5.3 \pm 0.5$
A6 (48 h)	$15 \pm 9$	$0.07 \pm 0.03$	$269 \pm 14$	$-155 \pm 9$	$4.8 \pm 0.4$

( $-2.0$ – $2.0 \text{ V (vs. SCE)}$ ) scanning curves in Fig. 4a–c, five obvious anode current peaks could be observed in the 1st scanning cycle:  $a_1$  ( $-1.38 \text{ V (vs. SCE)}$ ) corresponds to the reaction of Ti to  $\text{Ti}^{2+}$ ,  $a_2$  ( $-1.1 \text{ V (vs. SCE)}$ ) corresponds to the transition from  $\text{Ti}^{2+}$  to  $\text{Ti}^{3+}$  and  $a_3$  ( $-0.59 \text{ V (vs. SCE)}$ ) corresponds to the transition from  $\text{Ti}^{3+}$  to  $\text{Ti}^{4+}$  [24]. The related reactions are as follows [25]:



An overlapping anodic current peak ( $a_4$ ) at about  $0.3 \text{ V (vs. SCE)}$  could be seen, which corresponds to the transformation process from Ni to  $\text{Ni}^{2+}$  [26], and the possible reactions of Ni to  $\text{Ni}^{2+}$  in  $\text{Cl}^-$ -containing solution are as follows [27]:



When the potential is positive at 0.6 V (vs. SCE) and triggering an oxygen evolution process, a wide and flat anodic current range  $a_5$  can be observed. Four peaks can be observed in the backward scanning curves, among which  $c_1$  (1.25 V) is the reduction peak corresponding to  $a_5$ ,  $c_2$  (−0.91 V) relates to the peak of  $a_3$ ,  $c_3$  (−0.74 V) is the reduction peak of  $a_2$  and  $c_4$  (−1.34 V (vs. SCE)) is the

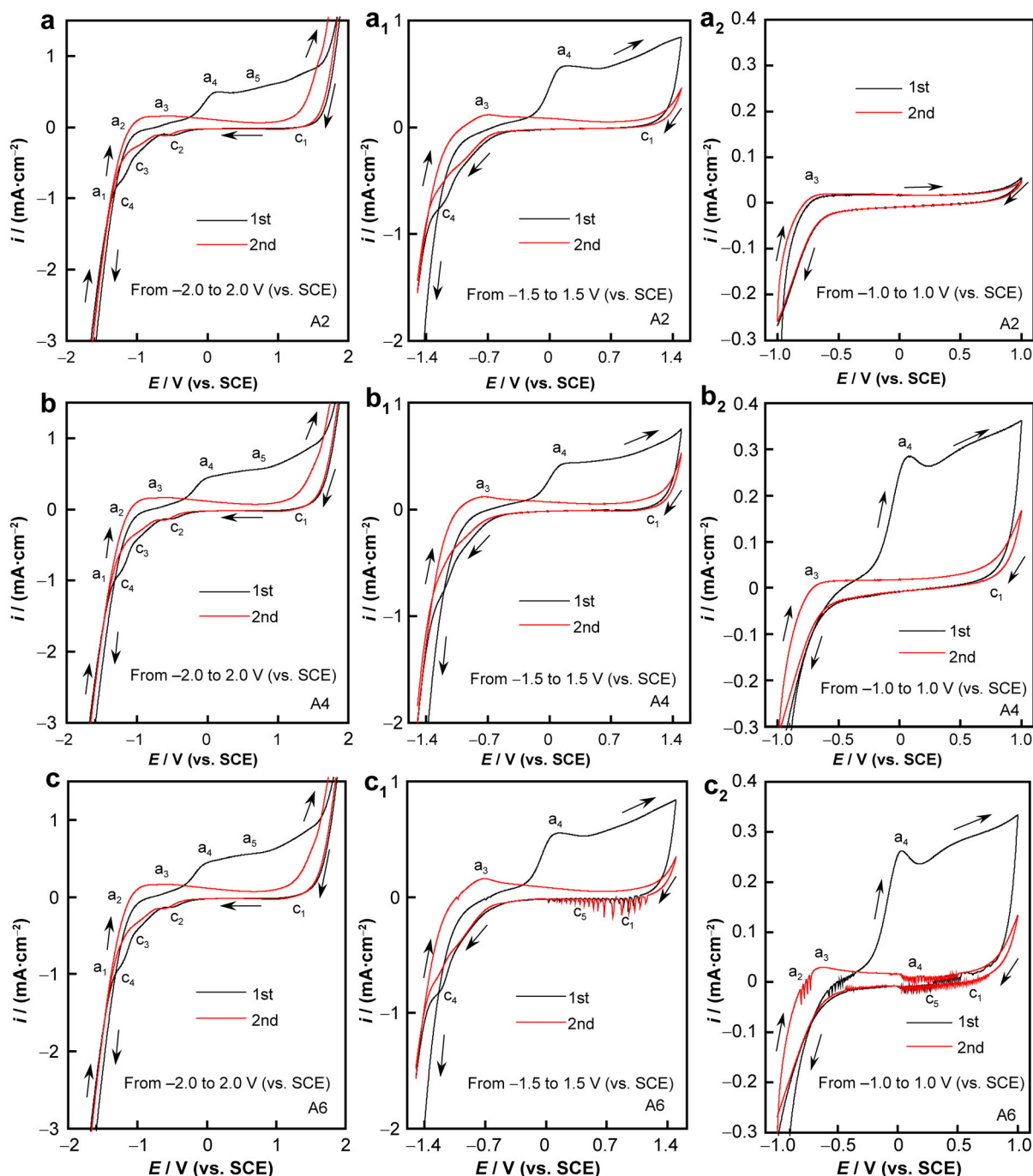


**Fig. 4** CV curves of L-PBF NiTi after immersion in artificial saliva for 30 min: **a**, **a**<sub>1</sub>, **a**<sub>2</sub> A2 (56 J·mm<sup>−3</sup>), **b**, **b**<sub>1</sub>, **b**<sub>2</sub> A4 (87 J·mm<sup>−3</sup>) and **c**, **c**<sub>1</sub>, **c**<sub>2</sub> A6 (60 J·mm<sup>−3</sup>)



reduction peak of  $a_1$ . The reduction peak of Ni cannot be observed, indicating that Ni is directly dissolved into the solution in the anode scanning and does not reduce in passive film of back scanning. Obvious anodic peak  $a_3$  and its reduction peak  $c_2$  can be observed in the scanning curve of the 2nd cycle, indicating that  $Ti^{4+}$  oxides are mainly formed, which is consistent with the conclusion that the outer layer of NiTi-SMA is mainly  $TiO_2$  [8, 9].

When the potential range is shortened to  $-1.5$ – $1.5$  V (vs. SCE), an obvious anodic peak  $a_4$  can be seen for A2, A4 and A6 in the 1st scan cycle, but there is no corresponding reduction peak for A2 and A4 in the backward curves. However, for A6, the small reduction peak of  $c_5$  can be seen in both the 1st and 2nd scan cycles, indicating that the stability of Ni in passive film of A6 is reduced. When the potential range is further shortened to  $-1.0$ – $1.0$  V (vs. SCE), no obvious Ni peaks can be observed in the 1st and 2nd scanning of A2. The scanning result of A4 is the same as that of scanned at  $-1.5$ – $1.5$  V (vs. SCE), but the intensity of peak  $a_4$  in the 1st cycle increases. In addition to the previous observed Ni peaks ( $a_4$ ,  $c_5$ ) at  $-1.5$ – $1.5$  V (vs. SCE) in A6, the anodic scanning peaks of  $a_2$  in the 1st circle and  $a_3$  in the 2nd cycle are also enhanced, indicating that Ti is also unstable in the passive film. In conclusion, the different potential range cyclic voltammetry scanning results show that the stability order of L-PBF NiTi passive films from high to low is: A2 > A4 > A6.

### 3.2.4 Electrochemical impedance spectroscopy

In order to further study the corrosion resistance and passive film formation process of L-PBF NiTi, EIS measurements at different immersion time (0.5, 6, 12, 24, 48, 72, 96, 120, 148 and 168 h) were performed. Figure 5 shows the representative Nyquist (Fig. 5a–c) and Bode (Fig. 5a<sub>1</sub>–c<sub>1</sub>) plots of L-PBF NiTi immersion in artificial saliva for 0.5, 24 and 168 h. It can be seen from the Nyquist diagram that the semicircle of L-PBF NiTi increases with immersion time. The Bode diagram of A2 shows one capacitance arc immersed for 0.5 h. Subsequently, broad capacitance arcs possibly appears in the low–middle-frequency region ( $1 \times 10^2$ – $1 \times 10^{-1}$ ), indicating a superposition of two time constants, and a diffusion impedance with a slope of about  $45^\circ$  in the low-frequency region ( $1 \times 10^{-1}$ – $1 \times 10^{-2}$ ). The Bode diagram of A4 shows one capacitance arc immersed at 0.5 h and then a wide capacitance arc (24 h) appears in the low–middle-frequency region ( $1 \times 10^2$ – $1 \times 10^{-1}$ ), indicating the superposition of two time constants. After immersion for 168 h, the two capacitance arcs can be clearly observed. The same as A4, the Bode diagram of A6 shows one capacitance arc at early stages of immersion (0.5 h), and then an overlapped broad capacitance arc with two superimposed time constants in

the low–middle-frequency region ( $1 \times 10^2$ – $1 \times 10^{-1}$ ) can be observed.

The potentiodynamic polarization (Fig. 3) and cyclic voltammetry (Fig. 4) tests demonstrate passive films formation on the three L-PBF NiTi during immersion, but according to the surface morphology analysis in Fig. 1, the initial surface integrity defects on the A4 and A6 samples may affect the passive film formation process. Therefore, we adopt three different equivalent electrical circuit (EEC) models to fit the EIS data. The EEC used for EIS parameter fitting to study the passive behavior of NiTi and related alloys [28–32] is shown in Fig. 6a–c. From the previous OCP (Fig. 2d) and potentiodynamic polarization (Fig. 3) test results, it can be deduced that the passive film formed in the early stage has relatively weak corrosion resistance. EIS of the sample immersed for 0.5 h was fitted with an equivalent circuit with one time constant as shown in Fig. 6a, wherein  $R_s$  represents the solution resistance from the reference electrode to the working electrode,  $R_b$  is the passive film resistance formed in the early stage and  $Q_b$  represents the capacitance of the passive film. With the extension of immersion time, a more corrosion resistant passive film will be formed. The two time constants equivalent circuit shown in Fig. 6c was used for A4 and A6 sample with immersion for 6–168 h. Due to the prolonged immersion time, a more corrosion resistant passive film with a dense inner layer and defect-containing outer layer is formed on the alloy surface,  $R_p$  and  $Q_p$  represent the defect-containing outer layer resistance and film capacitance, respectively [28],  $R_b$  is the inner passive film resistance and  $Q_b$  represents the inner passive film capacitance. Since the A2 sample exhibits a diffusion impedance in the low-frequency region (Fig. 5a and a<sub>1</sub>) at 6–168 h immersion, an equivalent circuit with a Warburg impedance ( $W$ ) in series with  $R_b$  was adopted (Fig. 6c) [31].

ZsimpWin 3.5 software was applied to fit the EIS results, and the quality of the fitted parameters was evaluated by the Chi-squared value. In general, the capacitance of the double electrode layer is not an ideal capacitance because of the roughness of the electrode surface. The impedance of the double electrode layer ( $Z_{Qdl}$ ) is related to the angular frequency of the excitation signal, which can be written as follows [33]:

$$Z_{Qdl} = \frac{1}{Y_0(j\omega)^n} \quad (11)$$

where  $\omega$  is the angular frequency,  $Y_0$  is a constant,  $j$  is the symbol of an imaginary number and  $n$  is the exponent of the constant phase element.  $n$  usually ranges from 0.5 to 1. When  $n = 1$ , the constant phase element is equivalent to the capacitance, the pit defect and the barrier layer (passive film) constant phase angle element  $Q_f$  and  $Q_b$  have similar meanings [31, 32].

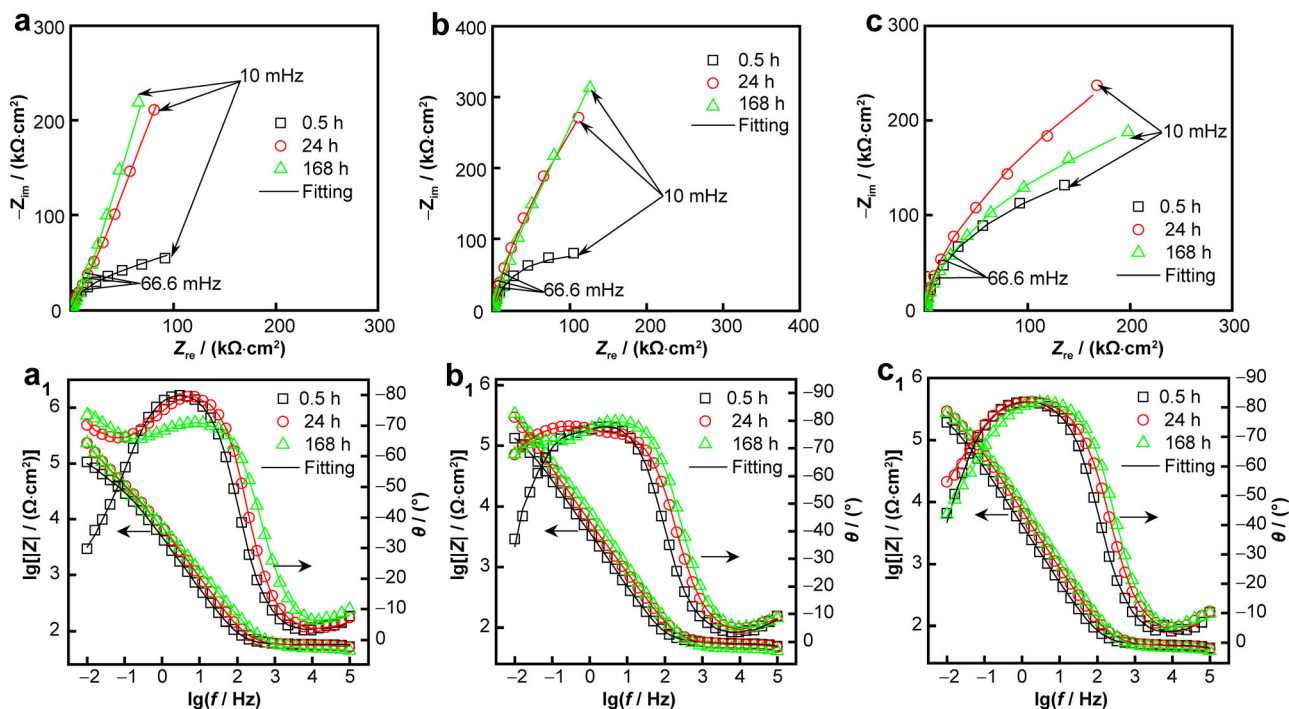


**Fig. 5** **a–c** Nyquist and **a<sub>1</sub>–c<sub>1</sub>** Bode diagrams of L-PBF NiTi after immersion in artificial saliva for different times: **a, a<sub>1</sub>**: A2 (56 J·mm<sup>-3</sup>); **b, b<sub>1</sub>**: A4 (87 J·mm<sup>-3</sup>) and **c, c<sub>1</sub>**: A6 (60 J·mm<sup>-3</sup>)

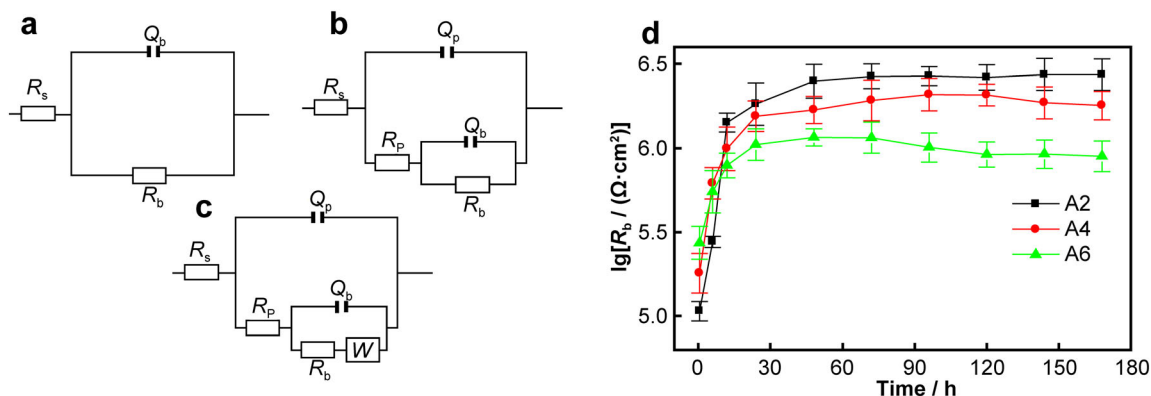


**Fig. 6** **a** Equivalent circuit of immersion for 0.5 h, **b** equivalent circuit of A2 immersion for 6–168 h and **c** equivalent circuit of A4 and A6 immersion for 6–168 h. **d**  $R_b$  of L-PBF NiTi after immersion in artificial saliva for different time (0.5, 6, 12, 24, 48, 72, 96, 120, 148 and 168 h)

The Warburg impedance can be written as follows [32]:

$$Z_w^{-1} = \sigma \sqrt{j\omega} \quad (12)$$

where  $\sigma$  represents the Warburg capacitance on the basis of the diffusion coefficient and the concentration of oxidized and reduced surface species.

It can be seen from the fitting values in Tables 3–5 that the solution resistance  $R_s$  changes little, which is in the range of 56.5–44.3  $\Omega\cdot\text{cm}^2$  and decreases with immersion time, probably related to ion release in the electrolyte. The outer defect-containing passive film resistance value  $R_p$  (order  $1 \times 10^2$ – $1 \times 10^4 \Omega\cdot\text{cm}^2$ ) is much smaller than that

of  $R_b$  (order  $1 \times 10^5$ – $1 \times 10^6 \Omega\cdot\text{cm}^2$ ). This indicates that the corrosion resistance of the outer layer is smaller, the inner layer has relatively good corrosion resistance, which is consistent with the previous published works [28, 31, 34]. These prior findings all show that the outer layer resistance value is usually within the order of  $1 \times 10^2$ – $1 \times 10^4 \Omega\cdot\text{cm}^2$ . Figure 6d shows the fitted  $R_b$  variation with immersion time; the  $R_b$  is in the following order: A6 > A4 > A2 after 0.5 h immersion, which is consistent with the potentiodynamic polarization curve fitting results (Fig. 3). For 6 h immersion,  $R_b$  value of A4 exceeds A6 in the order of A4 > A6 > A2. After 12 h

**Table 3** EIS parameter fitting values of A2 ( $56 \text{ J}\cdot\text{mm}^{-3}$ ) after immersed in artificial saliva for different time (0.5, 6, 12, 24, 48, 72, 96, 120, 148 and 168 h)

Time / h	$R_s /$ ( $\Omega\cdot\text{cm}^2$ )	$Q_f$		$R_p /$ ( $\text{k}\Omega\cdot\text{cm}^2$ )	$Q_b$		$R_b /$ ( $\text{k}\Omega\cdot\text{cm}^2$ )	$W /$ ( $10^4 \Omega\cdot\text{cm}^2\cdot\text{s}^{-0.5}$ )	Chi-squared / $10^{-4}$
		$Y_0 /$ ( $10^{-5} \Omega^{-1}\cdot\text{cm}^{-2}\cdot\text{s}^n$ )	$n$		$Y_0 /$ ( $10^{-5} \Omega^{-1}\cdot\text{cm}^{-2}\cdot\text{s}^n$ )	$n$			
0.5	56.7	—	—	—	4.3	—	0.90	107	11
6	57.2	3.3	0.95	37.1	4.2	—	0.84	277	2.5
12	57.5	2.4	0.93	38.7	2.9	—	0.81	1422	3.3
24	56.5	2.4	0.93	40.8	2.8	—	0.81	1830	3.5
48	55.5	2.4	0.92	29.8	2.7	—	0.80	2499	1.6
72	53.1	2.5	0.90	27.2	2.6	—	0.75	2669	1.5
96	51.6	2.5	0.89	21.2	2.5	—	0.75	2681	2.1
120	50.2	2.5	0.87	22.8	2.4	—	0.76	2631	1.9
144	48.3	2.5	0.86	20.3	2.2	—	0.95	2739	5.1
168	47.2	2.6	0.83	23.1	2.2	—	0.95	2737	4.1

**Table 4** EIS parameter fitting values of A4 ( $87 \text{ J}\cdot\text{mm}^{-3}$ ) after immersed in artificial saliva for different time (0.5, 6, 12, 24, 48, 72, 96, 120, 148 and 168 h)

Time / h	$R_s /$ ( $\Omega\cdot\text{cm}^2$ )	$Q_f$		$R_p /$ ( $\Omega\cdot\text{cm}^2$ )	$Q_b$		$R_b /$ ( $\text{k}\Omega\cdot\text{cm}^2$ )	Chi-squared / $10^{-4}$
		$Y_0 /$ ( $10^{-4} \Omega^{-1}\cdot\text{cm}^{-2}\cdot\text{s}^n$ )	$n$		$Y_0 /$ ( $10^{-5} \Omega^{-1}\cdot\text{cm}^{-2}\cdot\text{s}^n$ )	$n$		
0.5	55.5	—	—	—	5.5	—	0.90	180
6	54.3	3.9	0.89	504	4.9	—	0.90	617
12	53.9	3.5	0.74	336	3.7	—	0.88	989
24	45.7	4.2	0.83	427	3.5	—	0.87	1544
48	46.4	2.3	0.71	483	3.2	—	0.87	1687
72	44.7	2.0	0.68	692	3.0	—	0.87	1921
96	45.2	2.7	0.71	981	3.0	—	0.86	2084
120	46.0	1.6	0.99	1075	2.9	—	0.86	2066
144	45.6	0.99	0.99	3689	2.9	—	0.89	1859
168	44.9	0.82	0.97	7552	2.8	—	0.89	1790

immersion,  $R_b$  value of A2 is the largest, exceeding those of A4 and A6, and at this time, the order is  $A2 > A4 > A6$ . The Warburg impedance in the low frequency for A2 may be caused by ion migration during the formation of inner passive film, the value of Warburg impedance also increases with immersion time (Table 4), indicating that the effect of impeding ion migration is enhanced [35].

The corrosion resistance of L-PBF NiTi is comparable to that of the as-received base NiTi-SMA in the literature [30, 36–38]. The  $R_b$  of as-received NiTi-SMA supplied by manufacturers and under various surface treatments is generally within the range of  $1.2 \times 10^6$ – $2 \times 10^5 \Omega\cdot\text{cm}^2$ . The  $R_b$  of A2, A4 and A6 tested after 168 h is  $2.7 \times 10^6$ ,  $1.8 \times 10^6$  and  $8.9 \times 10^5 \Omega\cdot\text{cm}^2$ , respectively, that is larger than those of NiTi-SMA reported in the literature. The

passive film formed at 0.5 h has a relatively poor corrosion resistance, but the corrosion resistance of A2 is 1.5 and 3.0 times more than that of A4 and A6 after 168 h immersion.

The passive film barrier layer capacitance  $C_b$  can be calculated by the following equation [33, 34]:

$$C_b = Q_b^{1/n} R_b^{(1-n)/n} \quad (13)$$

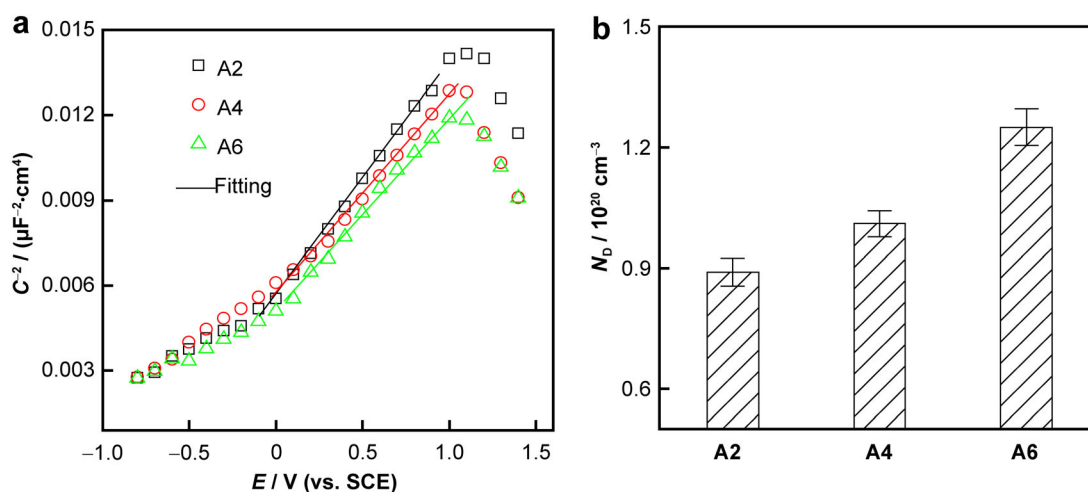
It is assumed that  $C_b$  is related to the thickness of passive film [34], such as:

$$C = \varepsilon \varepsilon_0 A / d \quad (14)$$

where  $\varepsilon$  is the dielectric constant of the film oxide, the typical dielectric constant of  $\text{TiO}_2$  is 100 [29] and  $\varepsilon_0$  is the dielectric constant in vacuum,  $\varepsilon_0 = 8.85 \times 10^{-12} \text{ F}\cdot\text{m}^{-1}$ .  $A$  is the effective area, and  $d$  is the film thickness. Based on

**Table 5** EIS parameter fitting values of A6 (60 J·mm<sup>-3</sup>) after immersed in artificial saliva for different time (0.5, 6, 12, 24, 48, 72, 96, 120, 148 and 168 h)

Time / h	$R_s / (\Omega \cdot \text{cm}^2)$	$Q_f$		$R_p / (\text{k}\Omega \cdot \text{cm}^2)$	$Q_b$		$R_b / (\text{k}\Omega \cdot \text{cm}^2)$	Chi-squared / $10^{-4}$
		$Y_0 / (10^{-5} \Omega^{-1} \cdot \text{cm}^{-2} \cdot \text{s}^n)$	$n$		$Y_0 / (10^{-5} \Omega^{-1} \cdot \text{cm}^{-2} \cdot \text{s}^n)$	$n$		
0.5	50.3	—	—	—	4.3	0.92	273	9.4
6	50.2	9.3	1.00	5.1	4.7	0.90	549	6.1
12	50.1	7.6	1.00	60.2	4.6	0.89	787	5.1
24	49.2	6.0	1.00	65.3	4.4	0.88	1048	6.1
48	48.5	5.7	1.00	72.1	3.8	0.88	1160	5.5
72	48.2	6.3	1.00	74.3	3.4	0.89	1153	4.4
96	47.5	5.8	1.00	76.8	3.3	0.89	1008	3.5
120	46.9	6.4	1.00	76.4	3.1	0.90	915	2.6
144	45.8	6.3	1.00	80.2	3.1	0.90	919	2.3
168	44.3	5.7	0.97	82.3	3.0	0.90	894	5.5

**Fig. 7** **a** Mott–Schottky curves and **b**  $N_D$  of L-PBF NiTi after immersed in artificial saliva for 168 h

the relationship between  $C$  and  $d$ , the smaller the  $C$ , the thicker the passive film. As can be seen from the  $Q_b$  values in Tables 3–5, the  $Q_b$  of L-PBF NiTi gradually decreases and tends to stabilize with immersion time, indicating that the thickness of inner passive film gradually thickens and tends to be constant.

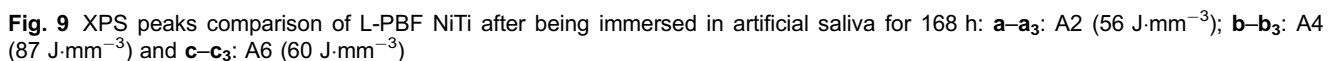
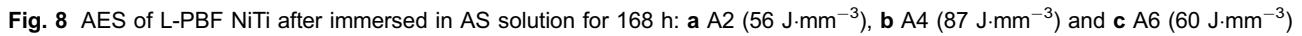
### 3.2.5 Mott–Schottky curve

Based on classical semiconductor theory, Mott–Schottky Eq. (15) can be used to describe the linear relationship between  $1/C^2$  and electrode potential [39, 40]. Figure 7a shows the Mott–Schottky curves of the three L-PBF NiTi immersed in artificial saliva for 168 h. When the electrode potential is higher than the flat band potential, the curves are all positive, indicating that the passive films of the L-

PBF NiTi formed in artificial saliva at OCP are n-type semiconductor, which again confirms that the passive film on the NiTi-SMA surface is mainly composed of  $\text{TiO}_2$  [29]. The donor carrier density in n-type semiconductors can be calculated based on Eq. (15) [40]:

$$\frac{1}{C^2} = \frac{2}{\varepsilon \varepsilon_0 e N_D} (E - E_{fb} - \frac{kT}{e}) \quad (15)$$

where  $C$  is the space charge layer capacitance of the oxide film;  $E$  is applied potential;  $\varepsilon_0$  is the vacuum dielectric constant and  $\varepsilon_0 = 8.85 \times 10^{-12} \text{ F} \cdot \text{m}^{-1}$ ;  $\varepsilon$  is the dielectric constant of the passive film, the typical dielectric constant  $\varepsilon$  of titanium oxide is 100 [29] and the vacuum dielectric constant  $\varepsilon_0$  is  $8.85 \times 10^{-12} \text{ F} \cdot \text{m}^{-1}$ ;  $e$  is the quantity of electrons,  $e = 1.602 \times 10^{-19} \text{ C}$ ;  $N_D$  is the electron donor concentration;  $E_{fb}$  is the flat band potential, which is the voltage intercept corresponding to the straight section of



As can be seen from the fitting results in Fig. 7b, the passive film defect concentration of the three L-PBF NiTi increases with a reduction of initial surface integrity (Fig. 1), and the average carrier density in the passive films

of A2, A4 and A6 is  $0.89 \times 10^{20}$ ,  $1.01 \times 10^{20}$  and  $1.25 \times 10^{20} \text{ cm}^{-3}$ , respectively. This is consistent with the study of the  $N_D$  of as-received NiTi within the order of  $1 \times 10^{20} \text{ cm}^{-3}$  [41], the  $N_D$  of A6 is much smaller than the minimum value ( $8 \times 10^{20} \text{ cm}^{-3}$ ) reported by Qiu et al. [39], which is 1.4 times more than that of the best performing A2.



**Table 6** Binding energies (eV) of major oxides peak values of L-PBF NiTi in passive film

Element	Peak	Species/binding energy
Ti	2p <sub>3/2</sub>	Ti (met)/454.1; TiO/454.6; Ti <sub>2</sub> O <sub>3</sub> /456.8; TiO <sub>2</sub> /458.8
	2p <sub>1/2</sub>	Ti (met)/460.1; TiO/460.2; Ti <sub>2</sub> O <sub>3</sub> /462.0; TiO <sub>2</sub> /464.3
Ni	2p <sub>3/2</sub>	Ni (met)/852.6; NiO/853.7; Ni(OH) <sub>2</sub> /856.2
O	1s	O <sup>2-</sup> /530.2; OH <sup>-</sup> /531.8; H <sub>2</sub> O/533

### 3.3 AES analysis

The AES results of L-PBF NiTi immersed in artificial saliva for 168 h are shown in Fig. 8. The two distinct-obvious layers can be observed on L-PBF NiTi with Ti rich in the outer layer and Ni rich in the inner layer. The outer layer of the L-PBF NiTi is mainly characteristic of Ti oxide. With the increase in sputtering depth, the content of O decreases rapidly, the content of Ti increases slowly and the content of Ni increases sharply and exceeds Ti at 7.1, 6.9 and 6.7 nm for A2, A4 and A6, respectively, indicating that Ni is mainly enriched in the inner layer of the passive film. The thickness of the passive film is generally at the location where the oxygen content is halved [42], which is 13.2, 9.7 and 8.7 nm for A2, A4 and A6, respectively. The passive film corrosion resistance is positively correlated with its thickness.

### 3.4 XPS analysis

AES analysis demonstrates that the outer layer of the L-PBF NiTi is mainly Ti oxides and the inner layer is mainly Ni oxides. The passive film thickness of three L-PBF NiTi is between 8.7 and 13.2 nm. In order to quantitatively analyze the difference between the two sub-layers, we analyzed the chemical composition of the outer layer of the original passive film and the inner layer after sputtering 6 nm. Figure 9 shows the XPS element composition analysis of the passive films of the three L-PBF NiTi samples immersed in artificial saliva for 168 h. As can be seen from the full spectra in Fig. 9a–c, the outer layer of the passive films of the three L-PBF NiTi is mainly composed of Ti and O. And obvious Ni peak could be detected in the inner layer of the passive films.

The peak value of the binding energy listed in Table 6 [43, 44] is used for L-PBF NiTi component fitting. Figure 9 a<sub>1</sub>–c<sub>1</sub> shows the oxide composition of Ni 2p<sub>3/2</sub> in the inner and outer layers of the passive film. In the outer passive films of L-PBF NiTi, only a very weak Ni metal (Ni (met)) (852.8 eV) signal can be detected. However, obvious Ni elements can be observed in the inner layer of the passive

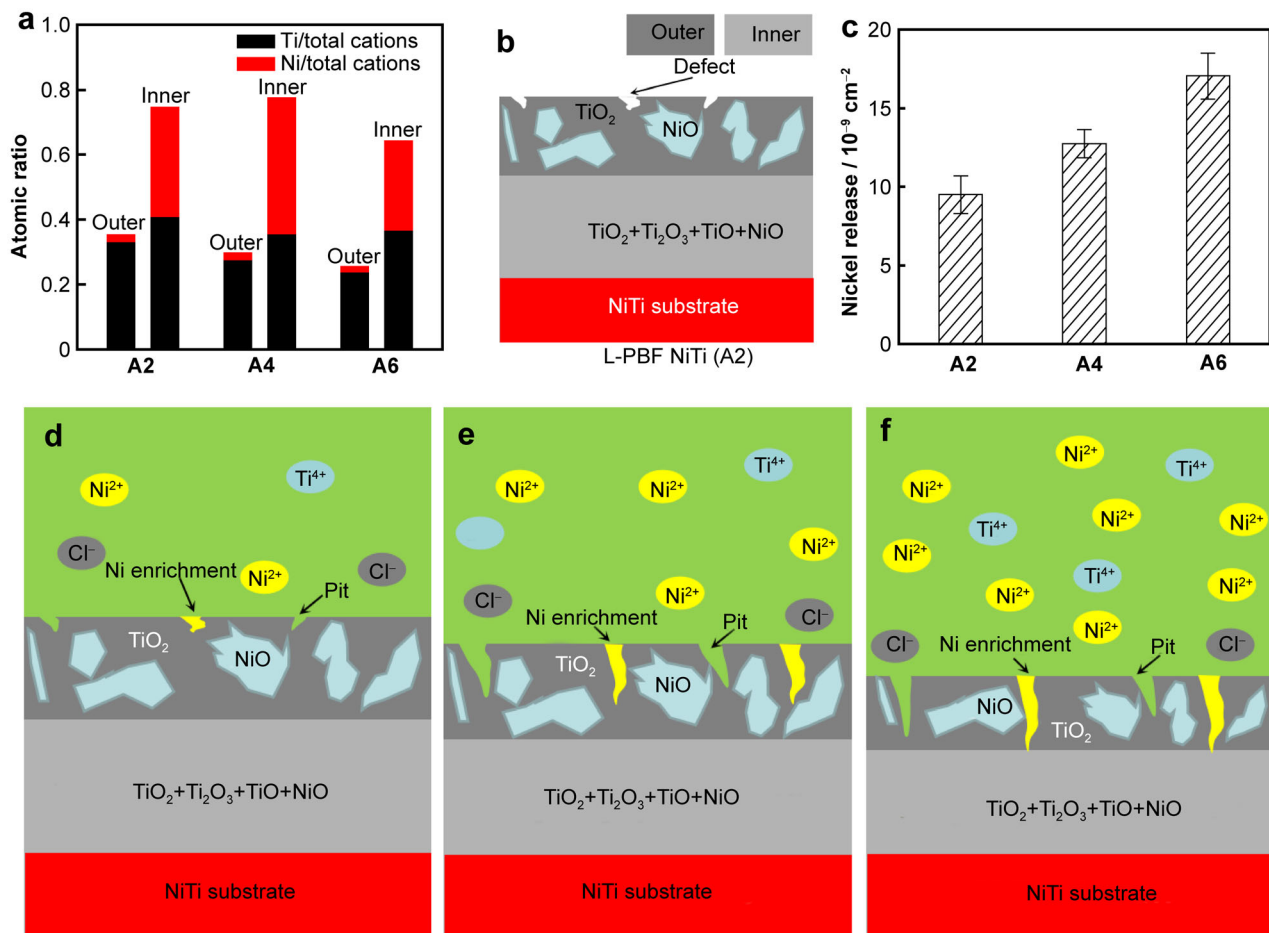
film of L-PBF NiTi. Ni is mainly Ni (met) and NiO, the content of Ni (met) is relatively higher than that of NiO. Figure 9a<sub>1</sub>–c<sub>1</sub> shows that Ni is mainly enriched in the inner layer of the passive film, and the relative higher Ni content in the outer layer of A6 passive film may be related to the defects in its passive film. As the content of NiO in the inner layer increases, the total amount of Ni is decreased.

Figure 9a<sub>2</sub>–c<sub>2</sub> shows the oxide composition of Ti in the inner and outer layers of the passive film. The outer passive films layers of the three L-PBF NiTi are mainly TiO<sub>2</sub> 2p<sub>3/2</sub> (458.8 eV) and TiO<sub>2</sub> 2p<sub>1/2</sub> (464.3 eV), and a small amount of TiO 2p<sub>3/2</sub> (454.6 eV) can also be detected, which again confirms that the outer passive film is mainly TiO<sub>2</sub>. Juan et al. [45] also showed that Ti<sup>4+</sup> was mainly in the outer layer of the passive film, Ti<sup>3+</sup> species were present in the inner passive film by first-principles calculation. A2 contains a small amount of TiO<sub>2</sub> 2p<sub>3/2</sub> (458.8 eV), Ti (met) 2p<sub>3/2</sub> (454.1 eV), Ti (met) 2p<sub>1/2</sub> (460.1 eV), TiO 2p<sub>3/2</sub> (454.6 eV), TiO 2p<sub>1/2</sub> (460.2 eV), Ti<sub>2</sub>O<sub>3</sub> 2p<sub>3/2</sub> (456.8 eV) and Ti<sub>2</sub>O<sub>3</sub> 2p<sub>1/2</sub> (462.0 eV). The Ti element distribution of A4 and A6 is similar to that of A2, in which the content of Ti (met) decreases, while the content of TiO and Ti<sub>2</sub>O<sub>3</sub> increases. Figure 10a and b shows that Ti is mainly enriched in the outer layer of the passive film. Although the Ti oxides decrease in the inner passive film, the content of Ti in the total cation content of the passive film remains high, which is beneficial for corrosion resistance [46].

Figure 9a<sub>3</sub>–c<sub>3</sub> shows the composition of O element in three L-PBF NiTi passive films. The O element is mainly composed of O<sup>2-</sup> (530.2 eV), OH<sup>-</sup> (531.8 eV) and H<sub>2</sub>O (533 eV). The content of O<sup>2-</sup> is the highest, which can be conformed to the Ti oxides (TiO, Ti<sub>2</sub>O<sub>3</sub> and TiO<sub>2</sub>) and Ni oxide (NiO) formation in the passive film.

### 3.5 Ni ion release rate

In actual orthodontic treatment, the release of Ni ions in NiTi-SMA can lead to clinical symptoms such as DNA cell damage of buccal mucosa and gingival tissue inflammation [3, 5, 9]. Figure 10c exhibits the Ni ion release concentration of the three L-PBF NiTi alloys immersed in artificial saliva for 168 h. The average value of the Ni ion release concentration of A2, A4 and A6 is  $9.5 \times 10^{-9}$ ,  $12.7 \times 10^{-9}$  and  $17.1 \times 10^{-9} \text{ cm}^{-2}$ , respectively, among which A2 is only 74.8% and 55.6% that of A4 and A6, respectively. According to Ni ion release concentrations reported by Briceno et al. [47], Wang et al. [11] and Huang et al. [48], the 1-week Ni ion release rate of NiTi-SMA in artificial saliva ranges from  $15 \times 10^{-9}$  to  $300 \times 10^{-9} \text{ cm}^{-2}$ . Obviously, the three L-PBF NiTi show limited Ni ion release, A6 ( $17.1 \times 10^{-9} \text{ cm}^{-2}$ ) in our experiment shows release rates very close to the lowest value in the literature ( $15 \times 10^{-9} \text{ cm}^{-2}$ ); A4



**Fig. 10** **a** XPS element content comparison of L-PBF NiTi after being immersed in artificial saliva for 168 h and **b** passive film section composition diagram, taking A2 (56 J·mm<sup>-3</sup>) as an example; **c** Ni ion release rate of L-PBF NiTi in artificial saliva for 168 h; schematic representation of passive layer build-up and Ni ion release of L-PBF NiTi in artificial saliva: **d** A2 (56 J·mm<sup>-3</sup>), **e** A4 (87 J·mm<sup>-3</sup>) and **f** A6 (60 J·mm<sup>-3</sup>)

( $12.7 \times 10^{-9} \text{ cm}^{-2}$ ) and A2 ( $9.5 \times 10^{-9} \text{ cm}^{-2}$ ) are 84.7% and 63.3% of that of the lowest value.

The difference in Ni ion release rate of the three L-PBF NiTi can be explained by the schematic representation shown in Fig. 10d–f. Based on the previous electrochemical testing (Figs. 3–7) and surface analysis (Figs. 8–10), an outer TiO<sub>2</sub>-rich and defect-containing double-layer passive film could be formed on the surface of L-PBF NiTi after immersion in artificial saliva. Ni ions will preferentially dissolve and release at the outer passive film defects [49]. The passive film of A2 has the highest corrosion resistance, which is related to the fact that A2 has fewer surface defects; thus, the amount of Ni ion precipitation is limited (Fig. 10d). Meanwhile, A6 has the largest number of defects in its surface, resulting in a relatively weak corrosion resistant passive film. As a result, the highest Ni ions release rate could be detected (Fig. 10f).

## 4 Conclusion

The corrosion behavior and passive film characteristics of three 3D-printed NiTi alloys fabricated by L-PBF with various  $E_v$  for A2 (56 J·mm<sup>-3</sup>), A4 (87 J·mm<sup>-3</sup>) and A6 (60 J·mm<sup>-3</sup>) were systematically investigated by means of electrochemical testing techniques, surface analysis and ion release studies with ICP-MS in artificial saliva. The main conclusions are as follows:

- (1) The OCP of L-PBF NiTi stabilizes rapidly with immersion time. The defects on the alloy surface can promote the formation rate of passive film in the early stage. The stability of Ni in passive films of  $E_v$  60 J·mm<sup>-3</sup> (A6) sample is relatively poor. A stable corrosion resistant passive film could be formed on the surface of  $E_v$  56 J·mm<sup>-3</sup> (A2) and 87 J·mm<sup>-3</sup> (A4) samples and stabilized in the order

of  $1 \times 10^6 \Omega \cdot \text{cm}^2$  after immersion for 24 h. The passive film corrosion resistance of L-PBF NiTi from high to low is: A2 > A4 > A6.

- (2) The L-PBF NiTi passive films show a two-layer structure with an outer Ti-rich ( $\text{TiO}_2$ ) layer and inner Ni- and Ti-rich layer. The contents of NiO and TiO increase with the increase in passive film thickness. The passive film thickness of the L-PBF NiTi ranges from 8.7 to 13.2 nm in the order of: A2 > A4 > A6.
- (3) The Ni ions release rate of the L-PBF NiTi in artificial saliva ranges from  $9.5 \times 10^{-9}$  to  $17.1 \times 10^{-9} \text{ cm}^{-2}$  and is in the order of A2 < A4 < A6, which is relatively low as compared to previously reported values ( $15 \times 10^{-9}$ – $300 \times 10^{-9} \text{ cm}^{-2}$ ) in the literature.
- (4) A2 prepared by L-PBF with linear energy density of  $0.2 \text{ J} \cdot \text{mm}^{-1}$  and volumetric energy density of  $56 \text{ J} \cdot \text{mm}^{-3}$  has the most uniform surface morphology, the best passive film corrosion resistance and the lowest Ni ion release rate.

**Acknowledgements** This study was financially supported by the financial support from the International Postdoctoral Exchange Fellowship Program 2019 by the Office of China Postdoctoral Council (No. 20190086) and the support from the Russian Science Foundation Grant (No. 19-79-30002).

## Declarations

**Conflict of interests** The authors declare that they have no conflict of interest.

**Open Access** This article is licensed under a Creative Commons Attribution 4.0 International License, which permits use, sharing, adaptation, distribution and reproduction in any medium or format, as long as you give appropriate credit to the original author(s) and the source, provide a link to the Creative Commons licence, and indicate if changes were made. The images or other third party material in this article are included in the article's Creative Commons licence, unless indicated otherwise in a credit line to the material. If material is not included in the article's Creative Commons licence and your intended use is not permitted by statutory regulation or exceeds the permitted use, you will need to obtain permission directly from the copyright holder. To view a copy of this licence, visit <http://creativecommons.org/licenses/by/4.0/>.

## References

- [1] Sharma N, Jangra KK, Raj T. Fabrication of NiTi alloy: a review. *Proc Inst Mech Eng, Part L: J Mater: Des Appl.* 2018; 232(3):250. <https://doi.org/10.1177/1464420715622494>.
- [2] Sharma N, Kumar K. Mechanical characteristics and bioactivity of porous  $\text{Ni}_{50-x}\text{Ti}_{50}\text{Cu}_x$  ( $x=0, 5$  and  $10$ ) prepared by P/M. *Mater Sci Technol: MST: publ Inst Metals.* 2018;34(7):934. <https://doi.org/10.1080/02670836.2017.1412041>.
- [3] Sun YH, Zhao Y, Zhao YY, Rong YJ, Yao HY, Yao XH, Huang RQ, Chu PK. Improving exposure of anodically ordered Ni-Ti-O and corrosion resistance and biological properties of NiTi alloys by substrate electropolishing. *Rare Met.* 2021;40(12):3575. <https://doi.org/10.1007/s12598-021-01721-4>.
- [4] Liu YL, Sun YH, Zhao Y, Li CL, Zhao FL, Yao XH, Hang RQ, Chu PK. Selective inhibition effects on cancer cells and bacteria of Ni-Ti-O nanoporous layers grown on biomedical NiTi alloy by anodization. *Rare Met.* 2022;41(1):78. <https://doi.org/10.1007/s12598-021-01707-2>.
- [5] Liu M, Li J, Zhang YX, Xue YN. Recent advances in corrosion research of biomedical NiTi shape memory alloy. *Rare Metal Mater Eng.* 2021;50(11):4165.
- [6] Sharma N, Singh G, Hegab H, Mia M, Batra NK. Tribo-corrosion characterization of NiTiCu alloy for bio-implant applications. *Mater Res Express.* 2019;6(9):096526. <https://doi.org/10.1088/2053-1591/ab2d95>.
- [7] Liu M, Hao YQ, Zheng LR, Niu L, Miao D. Role of coke in the passive properties of vitallium 2000 CoCrMo casting alloy in simulated oral environment. *J Mater Eng Perform.* 2019;28(12): 7527. <https://doi.org/10.1007/s11665-019-04469-2>.
- [8] Chen ZW, Gan CL, Qian JQ, Nong D. Effect of Cr content on phase transition characteristics and microhardness of near equiatomic NiTi SMA. *Chin J Rare Metals.* 2021;45(9):1034. <https://doi.org/10.13373/j.cnki.cjrm.XY20080009>.
- [9] Shanaghi A, Chu PK. Enhancement of mechanical properties and corrosion resistance of NiTi alloy by carbon plasma immersion ion implantation. *Surf Coat Technol.* 2018;365:52. <https://doi.org/10.1016/j.surfcoat.2018.04.027>.
- [10] Liu M, Zhu JN, Popovich VA, Borisov E, Mol JMC, Gonzalez-Garcia Y. Passive film formation and corrosion resistance of laser-powder bed fusion fabricated NiTi shape memory alloys. *J Market Res.* 2023;23:2991. <https://doi.org/10.1016/j.jmrt.2023.01.204>.
- [11] Wang J, Wang TR, Dong SJ, Kang XP, Zhao SY, Shi HY, Gao B, Ma SY, Liu M, Niu L, Zou R. The effect of Cu-doping on the corrosion behavior of NiTi alloy arch wires under simulated clinical conditions. *Mater Res Express.* 2021;8:016537. <https://doi.org/10.1088/2053-1591/abdb4e>.
- [12] Mirjalili M, Momeni M, Ebrahimi N, Moayed MH. Comparative study on corrosion behaviour of nitinol and stainless steel orthodontic wires in simulated saliva solution in presence of fluoride ions. *Mater Sci Eng C.* 2013;33(4):2084. <https://doi.org/10.1016/j.msec.2013.01.026>.
- [13] Mocnik P, Kosec T, Kovac J, Bizjak M. The effect of pH, fluoride and tribocorrosion on the surface properties of dental archwires. *Mater Sci Eng C.* 2017;78:682. <https://doi.org/10.1016/j.msec.2017.04.050>.
- [14] Masjedi MK, Niknam O, Jahromi NH, Javidi P, Rakhshan V. Effects of fixed orthodontic treatment using conventional, copper-included, and epoxy-coated nickel-titanium archwires on salivary nickel levels: a double-blind randomized clinical trial. *Biol Trace Elem Res.* 2016;174(1):27. <https://doi.org/10.1007/s12011-016-0690-7>.
- [15] Elahinia M, Moghaddam NS, Andani MT, Amerinatanzi A, Bimber BA, Hamilton RF. Fabrication of NiTi through additive manufacturing: a review. *Prog Mater Sci.* 2016;83:630. <https://doi.org/10.1016/j.pmatsci.2016.08.001>.
- [16] Chen X, Liu K, Guo W, Gangil N, Kononov SV. The fabrication of NiTi shape memory alloy by selective laser melting: a review. *Rapid Prototyp J.* 2019;25(8):1421. <https://doi.org/10.1108/RPJ-11-2018-0292>.
- [17] Wang C, Tan XP, Du Z, Chandra S, Sun Z, Li CWJ, Tor SB, Lim CS, Wong CH. Additive manufacturing of NiTi shape memory alloys using pre-mixed powders. *J Mater Process Technol.* 2019; 271:152. <https://doi.org/10.1016/j.jmatproc.2019.03.025>.
- [18] Khoo ZX, Liu Y, An J, Chua CK, Shen YF, Kuo CN. A review of selective laser melted NiTi shape memory alloy. *Materials.* 2018;11(4):519. <https://doi.org/10.3390/ma11040519>.



- [19] Marattukalam JJ, Singh AK, Datta S, Das M, Balla VK, Bontha S, Kalpathy SK. Microstructure and corrosion behavior of laser processed NiTi alloy. *Mater Sci Eng C*. 2015;57:309. <https://doi.org/10.1016/j.msec.2015.07.067>.
- [20] Zhu JN, Borisov E, Liang X, Farber E, Popovich VA. Predictive analytical modelling and experimental validation of processing maps in additive manufacturing of nitinol alloys. *Addit Manuf*. 2021;38:101802. <https://doi.org/10.1016/j.addma.2020.101802>.
- [21] Bayat M, Thanki A, Mohanty S, Witvrouw A, Yang SF, Jesper T, Tiedje NS, Hattel JH. Keyhole-induced porosities in laser-based powder bed fusion (L-PBF) of Ti6Al4V: high-fidelity modelling and experimental validation. *Addit Manuf*. 2019;30:100835. <https://doi.org/10.1016/j.addma.2019.100835>.
- [22] Haleem SMAE, Aal EEAE, Wanees SAE, Diab A. Environmental factors affecting the corrosion behaviour of reinforcing steel: I. The early stage of passive film formation in  $\text{Ca}(\text{OH})_2$  solutions. *Corros Sci*. 2010;52(12):3875. <https://doi.org/10.1016/j.corsci.2010.07.035>.
- [23] Liu M, Cheng XQ, Li XG, Pan Y, Li J. Effect of Cr on the passive film formation mechanism of steel rebar in saturated calcium hydroxide solution. *Appl Surf Sci*. 2016;389(15):1182. <https://doi.org/10.1016/j.apsusc.2016.08.074>.
- [24] Yang XJ, Du CW, Wan HX, Liu ZY, Li XG. Influence of sulfides on the passivation behavior of titanium alloy TA2 in simulated seawater environments. *Appl Surf Sci*. 2018;458:198. <https://doi.org/10.1016/j.apsusc.2018.07.068>.
- [25] Parsons R. Atlas of electrochemical equilibria in aqueous solutions. *J Electroanal Chem*. 1967;13(4):471. [https://doi.org/10.1016/0022-0728\(67\)80059-7](https://doi.org/10.1016/0022-0728(67)80059-7).
- [26] Ayoub H, Griveau S, Lair V, Brunswick P, Cassir M, Bedioui F. Electrochemical characterization of nickel electrodes in phosphate and carbonate electrolytes in view of assessing a medical diagnostic device for the detection of early diabetes. *Electroanalysis*. 2010;22(21):2483. <https://doi.org/10.1002/elan.201000307>.
- [27] Milosev I, Kosec T. Study of Cu-18Ni-20Zn nickel silver and other Cu-based alloys in artificial sweat and physiological solution. *Electrochim Acta*. 2007;52:6799. <https://doi.org/10.1016/j.electacta.2007.04.105>.
- [28] Sun XT, Kang ZX, Zhang XL, Jiang HJ, Guan RF, Zhang XP. A comparative study on the corrosion behavior of porous and dense NiTi shape memory alloys in NaCl solution. *Electrochim Acta*. 2011;56(18):6389. <https://doi.org/10.1016/j.electacta.2011.05.019>.
- [29] Figueira N, Silva TM, Carmezim MJ, Fernandes JCS. Corrosion behaviour of NiTi alloy. *Electrochim Acta*. 2009;54(3):921. <https://doi.org/10.1016/j.electacta.2008.08.001>.
- [30] Chembath M, Balaraju JN, Sujata M. Surface characteristics, corrosion and bioactivity of chemically treated biomedical grade NiTi alloy. *Mater Sci Eng C*. 2015;56:417. <https://doi.org/10.1016/j.msec.2015.06.051>.
- [31] Freitag M, Osiewicz B, Goryczka T, Lelątko J. Application of EIS to study the corrosion resistance of passivated NiTi shape memory alloy in simulated body fluid. *Solid State Phenom*. 2012;183:57. <https://doi.org/10.4028/www.scientific.net/SSP.183.57>.
- [32] Wang R, Luo SJ, Liu M, Xue YN. Electrochemical corrosion performance of Cr and Al alloy steels using a J55 carbon steel as base alloy. *Corros Sci*. 2014;85:270. <https://doi.org/10.1016/j.corsci.2014.04.023>.
- [33] Liu M, Cheng XQ, Li XG, Lu TJ. Corrosion behavior of low-Cr steel rebars in alkaline solutions with different pH in the presence of chlorides. *J Electroanal Chem*. 2017;803(15):40. <https://doi.org/10.1016/j.jelechem.2017.09.016>.
- [34] Barros C, Gomes J. Strain induced localized corrosion of NiTi, NiTiCo and NiTiCr alloys in 0.9% NaCl. *J Mech Behav Biomed Mater*. 2020;112:104015. <https://doi.org/10.1016/j.jmbbm.2020.104015>.
- [35] Yang DZ, Liu CL, Liu XP, Qi M, Lin GQ. EIS diagnosis on the corrosion behavior of TiN coated NiTi surgical alloy. *Curr Appl Phys*. 2005;5(5):417. <https://doi.org/10.1016/j.cap.2004.11.002>.
- [36] Bolat G, Mareci D, Iacoban S, Cimpoeu N, Munteanu C. The estimation of corrosion behavior of NiTi and NiTiNb alloys using dynamic electrochemical impedance spectroscopy. *J Spectrosc*. 2013. <https://doi.org/10.1155/2013/714920>.
- [37] Michalska J, Sowa M, Socha RP, Simka W, Beata C. The influence of desulfovibrio desulfuricans bacteria on a Ni-Ti alloy: electrochemical behavior and surface analysis. *Electrochim Acta*. 2017;249:135. <https://doi.org/10.1016/j.electacta.2017.08.024>.
- [38] Trollic IM, Serdarevic NL, Todoric Z, Budimir A, Spalj S, Curkovic HO. Corrosion of orthodontic archwires in artificial saliva in the presence of lactobacillus reuteri. *Surf Coat Technol*. 2019;370:44. <https://doi.org/10.1016/j.surfcoat.2019.04.081>.
- [39] Qiu P, Gao PP, Wang SY, Li ZH, Qing YY, Zhang QQ, Xiong ZW, Hao SJ. Study on corrosion behavior of the selective laser melted NiTi alloy with superior tensile property and shape memory effect. *Corros Sci*. 2020;175(11):108891. <https://doi.org/10.1016/j.corsci.2020.108891>.
- [40] Liu M, Li J, Li DP, Zheng LR. The passive properties of TA10 in coca-cola containing oral environment. *Anti-Corros Methods Mater*. 2021;68(1):9. <https://doi.org/10.1108/ACMM-05-2020-2312>.
- [41] Lv JL, Liang TX, Wang C, Dong L. Surface corrosion enhancement of passive films on NiTi shape memory alloy in different solutions. *Mater Sci Eng C*. 2016;63:192. <https://doi.org/10.1016/j.msec.2016.02.066>.
- [42] Luo H, Su H, Dong CF, Xiao K, Li XG. Electrochemical and passivation behavior investigation of ferritic stainless steel in alkaline environment. *Constr Build Mater*. 2015;96:502. <https://doi.org/10.1016/j.conbuildmat.2015.08.052>.
- [43] Alqarni ND, Wysocka J, El-Bagoury N, Ryl J, Amin MA, Boukherroub R. Effect of cobalt addition on the corrosion behavior of near equiatomic NiTi shape memory alloy in normal saline solution: electrochemical and XPS studies. *RSC Adv*. 2018;8(34):19289. <https://doi.org/10.1039/C8RA02031K>.
- [44] Rudolf R, Stamboli A, Kocijan A. Atomic layer deposition of a  $\text{TiO}_2$  layer on nitinol and its corrosion resistance in a simulated body fluid. *Metals*. 2021;11:659. <https://doi.org/10.3390/met11040659>.
- [45] Juan J, Orazi V, Sandoval M, Bechthold P, Hernandez-Laguna A, Sainz-Diaz CI. DFT study of Ni segregation at the B2-NiTi(110)/rutile- $\text{TiO}_2$ (110) interface. *Appl Surf Sci*. 2019;489:287. <https://doi.org/10.1016/j.apsusc.2019.05.336>.
- [46] Wang L, Yu H, Wang SY, Chen B, Wang YH, Fan WQ, Sun DB. Quantitative analysis of local fine structure on diffusion of point defects in passive film on Ti. *Electrochim Acta*. 2019;314:161. <https://doi.org/10.1016/j.electacta.2019.05.048>.
- [47] Briceno J, Romeu A, Espinar E, Llamas JM, Gil FJ. Influence of the microstructure on electrochemical corrosion and nickel release in NiTi orthodontic archwires. *Mater Sci Eng C*. 2013;33(8):4989. <https://doi.org/10.1016/j.msec.2013.08.024>.
- [48] Huang HH, Chiu YH, Lee TH, Wu SC, Yang HW, Su KH. Ion release from NiTi orthodontic wires in artificial saliva with various acidities. *Biomaterials*. 2003;24(20):3585. [https://doi.org/10.1016/S0142-9612\(03\)00188-1](https://doi.org/10.1016/S0142-9612(03)00188-1).
- [49] Asserghine A, Medvidović-Kosanović M, Nagy L, Nagy E. In situ monitoring of the transpassivation and repassivation of the passive film on nitinol biomaterial by scanning electrochemical microscopy. *Electrochem Commun*. 2019;107:106539. <https://doi.org/10.1016/j.elecom.2019.106539>.